# CONSTRUCTING A *WISE* HIGH RESOLUTION GALAXY ATLAS

T. H. Jarrett[1], F. Masci[1], C. W. Tsai[1], S. Petty[2], M. Cluver[3], Roberto J. Assef[4,11], D. Benford[5], A. Blain[6],
C. Bridge[7], E. Donoso[8], P. Eisenhardt[4], J. Fowler[1], B. Koribalski[9], S. Lake[2], James D. Neill[7],
M. Seibert[10], K. Sheth[11], S. Stanford[12], and E. Wright[2]
[1] Infrared Processing and Analysis Center (IPAC), California Institute of Technology, Pasadena, CA 91125, USA; jarrett@ipac.caltech.edu
[2] Physics and Astronomy Department, University of California, Los Angeles, CA 90095, USA
[3] Australian Astronomical Observatory, P.O. Box 296, Epping, NSW 1710, Australia
[4] Jet Propulsion Laboratory, California Institute of Technology, 4800 Oak Grove Drive, Mail Stop 169-221, Pasadena, CA 91109, USA
[5] NASA Goddard Space Flight Center, Code 665, Greenbelt, MD 20771, USA
[6] Department of Physics and Astronomy, University of Leicester, LE1 7RH Leicester, UK
[7] Department of Astronomy, California Institute of Technology, Pasadena, CA 91125, USA
[8] Spitzer Science Center, IPAC, California Institute of Technology, Pasadena, CA 91125, USA
[9] CSIRO Astronomy & Space Science, Australia Telescope National Facility (ATNF), P.O. Box 76, Epping, NSW 1710, Australia
[10] Observatories of the Carnegie Insititution for Science, 813 Santa Barbara Street, Pasadena, CA 91101, USA
[11] NRAO, 520 Edgemont Road, Charlottesville, VA 22903-2475, USA
[12] Department of Physics, University of California, One Shields Avenue, Davis, CA 95616, USA

## ABSTRACT

After eight months of continuous observations, the *Wide-field Infrared Survey Explorer* (*WISE*) mapped the entire sky at $3.4\,\mu$m, $4.6\,\mu$m, $12\,\mu$m, and $22\,\mu$m. We have begun a dedicated *WISE* High Resolution Galaxy Atlas project to fully characterize large, nearby galaxies and produce a legacy image atlas and source catalog. Here we summarize the deconvolution techniques used to significantly improve the spatial resolution of *WISE* imaging, specifically designed to study the internal anatomy of nearby galaxies. As a case study, we present results for the galaxy NGC 1566, comparing the *WISE* enhanced-resolution image processing to that of *Spitzer*, *Galaxy Evolution Explorer*, and ground-based imaging. This is the first paper in a two-part series; results for a larger sample of nearby galaxies are presented in the second paper.

*Key words:* galaxies: fundamental parameters – galaxies: statistics – infrared: galaxies – surveys – techniques: image processing

*Online-only material:* color figures

## 1. INTRODUCTION

For nearly three decades now, starting with *IRAS* in the early 1980s and continuing today with the *Spitzer* and the *AKARI Space Telescopes*, the infrared properties of galaxies have been explored at ever increasing sensitivity, spatial, and spectral resolution. The *Spitzer* Infrared Nearby Galaxies Survey (SINGS; Kennicutt et al. 2003) represents the "gold standard" study of nearby galaxies, employing every infrared instrument of *Spitzer* to study in detail the properties of 75 nearby "representative" galaxies. A larger *Spitzer* imaging sample is found in the SINGS follow-up project, Local Volume Legacy (LVL). Expanding the sample to several thousand galaxies, the *Spitzer* Survey of Stellar Structure in Galaxies (S4G; Sheth et al. 2010) continued the SINGS and LVL surveys through the two short (near-infrared) wavelength bands of IRAC (3.6 and 4.5 μm), focusing on the internal stellar structure of galaxies.

Following closely in succession to the *AKARI* all-sky survey (Murakami et al. 2007), the latest generation infrared space telescope, the *Wide-field Infrared Survey Explorer* (*WISE*), expands these powerful surveys through its all-sky coverage and megapixel cameras, capable of constructing large, diverse, and complete statistical samples—for both the near-infrared and mid-infrared windows—sensitive to both stellar structure (as with S4G) and interstellar processes (as with SINGS). *WISE* was specifically designed and optimized to detect and extract point-source information. Detection, for example, was carried out using co-addition of image frames that were constructed

with a resampling method based on a matched filter derived from the *WISE* point-spread function (PSF). As a consequence, this interpolation method tends to smear the images, making them less optimal for the detection and characterization of resolved sources. However, owing to the stable PSF for all four *WISE* bands, there is a way to apply deconvolution techniques to recover from the smearing and further improve the spatial resolution. In this first paper of a two-part series, we demonstrate how the angular resolution of *WISE* may be enhanced to achieve information on physical scales comparable to those of *Spitzer* imaging, which enable a detailed study of the internal anatomy of galaxies. We employ two enhancement methods: Variable-Pixel Linear Reconstruction, or "drizzle" using a simple top-hat kernel (drizzle factor of unity), and the maximum correlation method (HiRes-MCM; Masci & Fowler 2009), to construct the *WISE* High Resolution Galaxy Atlas (WHRGA), consisting of several thousand nearby galaxies.

The WHRGA will comprise a complete mid-infrared source catalog and high-resolution image atlas of the largest angular-sized galaxies in the local universe. In this first paper, we focus mostly on the maximum correlation method (MCM) algorithm, demonstrating its performance using *WISE*, *Spitzer*, and *Galaxy Evolution Explorer* (*GALEX*) imaging of a nearby spiral galaxy NGC 1566. In the second paper (Jarrett et al. 2012b; hereafter referred to as Paper II), we demonstrate the early results of the WHRGA project for a sample of 17 galaxies, all observed by *Spitzer* and *GALEX*, chosen to be of large angular size, diverse morphology, and covering a range in color, stellar mass, and star formation. In addition to basic photometry, source characterization, and surface brightness decomposition, Paper II

---

[11] NASA Postdoctoral Program Fellow.

**Table 1**
*WISE* Imaging Point-source Profile Widths for Stars in the NGC 1566 Field

| Method | W1 3.4 $\mu$m FWHM (arcsec) | W2 4.6 $\mu$m FWHM (arcsec) | W3 12 $\mu$m FWHM (arcsec) | W4 22 $\mu$m FWHM (arcsec) |
|---|---|---|---|---|
| Atlas | 8.4 | 9.2 | 11.4 | 18.6 |
| Enhanced (drizzle) | 5.9 | 6.5 | 7.0 | 12.4 |
| MCM-HiRes | 2.6 | 3.0 | 3.5 | 5.5 |

**Notes.** Atlas co-added images are the standard public release product of *WISE*. Variable-Pixel Linear Reconstruction, or "drizzle," and the MCM-HiRes method are part of the *WISE* High Resolution Galaxy Atlas. For comparison, the diffraction and optics-limited resolution of *WISE* single frame images is $\sim 6''$ for the short bands, and $\sim 12''$ for the 22 $\mu$m band.

also derives star formation rates (SFRs) and stellar masses using the global measurements.

This first paper is organized as follows. Section 2 provides more technical information about the *WISE* mission and data products. Section 3 provides the ancillary data used to compare to *WISE*, including *Spitzer* and *GALEX* imaging. In Section 4, we outline the MCM-HiRes image deconvolution method and illustrate its performance using a set of simulated observations. In Section 5, we focus on a case study of NGC 1566 to demonstrate the enhanced resolution performance using real *WISE* imaging datum comparing HiRes and "drizzle" reconstructions with ground-based and *Spitzer* imaging of NGC 1566. All reported magnitudes are in the Vega System (unless otherwise specified).

## 2. *WISE* MISSION AND DATA PRODUCTS

The NASA-funded Medium-Class Explorer mission, *WISE*, consists of a 40 cm space infrared telescope, whose science instrumentation includes 1024 × 1024 pixel Si:As and HgCdTe arrays, cooled with a two-stage solid hydrogen cryostat. Dichroic beam splitters allow simultaneous images in four mid-infrared bands, each covering a $47' \times 47'$ field of view. The duty cycle was 11 s, achieved using a scan mirror that stabilizes the line of sight while the spacecraft scans the sky, achieving an angular resolution of $\sim 6''$ in the short bandpasses and $\sim 12''$ in the longest bandpass. Multiple, overlapping frames are combined to form deeper co-added images. Launched in December of 2009 into a Sun-synchronous polar orbit, over a time span of eight months *WISE* completed its primary mission to survey the entire sky in the 3.4, 4.6, 12, and 22 $\mu$m infrared bands with 5$\sigma$ point-source sensitivities of at least 0.08, 0.11, 0.8, and 4 mJy, respectively (Wright et al. 2010), and considerably deeper sensitivities at higher ecliptic latitudes (Jarrett et al. 2011).

Detailed in the *WISE* Explanatory Supplement (Cutri et al. 2012),[12] "Atlas" images[13] are created from single-exposure frames that touch a pre-defined $1°56 \times 1°56$ footprint on the sky. For each band, a spatially registered image is produced by interpolating and co-adding multiple 7.7/8.8 s single-exposure images onto the image footprint. To suppress copious cosmic rays and other transient events that populate the single-exposure frames, time-variant pixel outlier rejection is used during the co-addition process. The resulting sky intensity "Atlas" mosaics are 4095 × 4095 pixels with $1''375$ pixel$^{-1}$ scale, providing a $1°56 \times 1°56$ wide field. The angular resolution of the resultant Atlas images is markedly larger, >40%, than the native resolution of *WISE* (see Table 1), primarily due to the mission requirement for optimal source detection (through kernel smoothing) at the

expense of angular resolution. In addition to the sky intensity mosaics, 1$\sigma$ uncertainty maps (tracking the error in intensity values) and depth-of-coverage maps are part of the standard products. The number of frames that are co-added depends on the field location relative to the ecliptic: those near the equator will have the lowest coverage (typically 12–14 frames), while those near the poles have the highest coverage ($\gg$1000 frames).

The *WISE* All-Sky public data release in 2012 March includes imaging and source catalogs, available through the Infrared Science Archive. It should be emphasized that the *WISE* Source Catalog is designed, optimized, and calibrated for point sources. The complexity of detecting and measuring resolved sources was beyond the resources of the *WISE* Science Data Center (WSDC) processing. As a consequence, the *WISE* archive and public release catalogs have either completely missed nearby galaxies or, even worse, their integrated fluxes are systematically underestimated (because they are measured as point sources) and often chopped into smaller pieces. However, the *WISE* public release imaging products do capture resolved and complex objects. One of the goals of this current study is to use new image products to characterize and assess the quality of source extraction for resolved galaxies observed by *WISE*. We apply image resolution-enhancement techniques and compare the resulting measurements with those extracted using *Spitzer* and *GALEX* imaging (Paper II).

## 3. ANCILLARY DATA

### 3.1. *Spitzer-SINGS* Imaging

In this first paper we focus on the spiral galaxy NGC 1566,[14] which was part of the *Spitzer*-SINGS survey of nearby galaxies. It is located at a distance of 9.5 Mpc (based on four separate Tully–Fisher measurements; Willick et al. 1997; Tully 1988), has a morphological class type of SAB(rs)bc, and includes a Seyfert 1 nucleus (NASA Extragalactic Database). The SINGS team has provided enhanced-quality spectroscopy and imaging mosaics that is available to the public through the Spitzer Data Archives.[15] For this work, we utilize *Spitzer*-IRAC and *Spitzer*-MIPS-24 imaging, which are fully calibrated with astrometry and photometric solutions. Additionally, the SINGS team has provided ancillary ground-based imaging, of which we use the optical *B*-band and H$\alpha$ data products.

### 3.2. *GALEX* Imaging

*GALEX* FUV (0.1516 $\mu$m) and NUV (0.2267 $\mu$m) images of NGC 1566 were obtained from the *GALEX* Medium Imaging Survey (MIS; Martin et al. 2005), which were processed using

---

[12] http://wise2.ipac.caltech.edu/docs/release/

[13] Public release *WISE* co-added images are referred to as "Atlas" images, available through http://irsa.ipac.caltech.edu/applications/wise/

[14] It has ecliptic coordinates of $32°07$, $-73°35$, which means it has very good coverage with *WISE*.

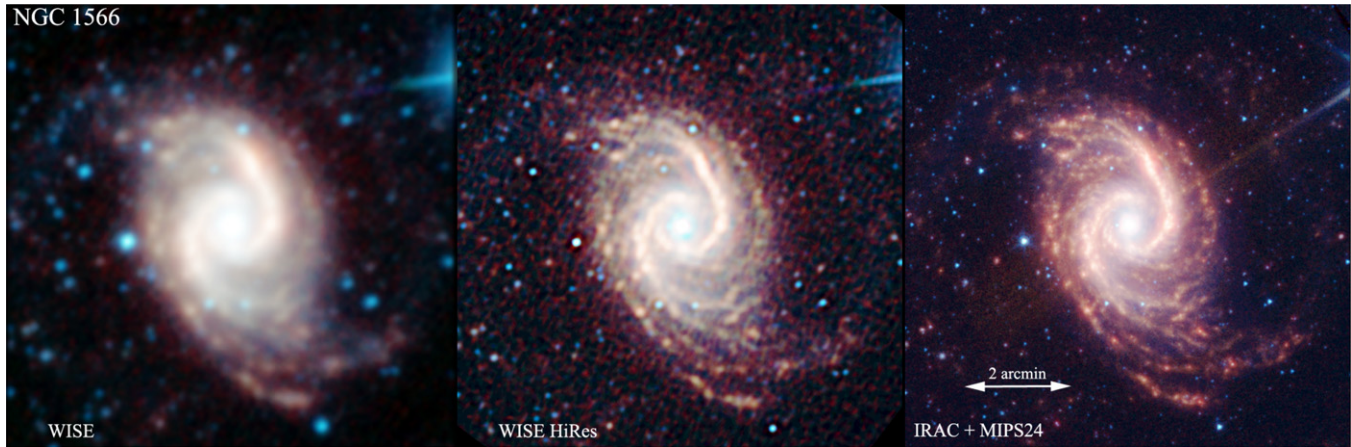[15] http://data.spitzer.caltech.edu/popular/sings/20070410_enhanced_v1/

**Figure 1.** *WISE* and *Spitzer* composite of NGC 1566. The left panel shows the nominal (public release, "Atlas") *WISE* mosaic, where the colors correspond to *WISE* bands: 3.4 $\mu$m (blue), 4.6 $\mu$m (green), 12.0 $\mu$m (orange), 22 $\mu$m (red). The middle panel shows the MCM-HiRes spatial resolution enhancement of the *WISE* mosaics. The right panel shows IRAC+MIPS mosaic, where the colors correspond to 3.6 $\mu$m (blue), 4.5 $\mu$m (green), 5.8 $\mu$m (yellow), 8.0 $\mu$m (orange), and 24 $\mu$m (red).
(A color version of this figure is available in the online journal.)

the standard *GALEX* pipeline (Morrissey et al. 2005, 2007). The MIS reaches a limiting NUV magnitude of 23 (AB mag) through multiple eclipse exposures that are typically 1 ks or greater in duration, while azimuthal averaging reaches surface brightness depths of $\sim$30–31 mag arcsec$^{-2}$ (AB mag).

### 4. *WISE* HIGH-RESOLUTION RECONSTRUCTION

The nominal spatial resolution of *WISE*, $\sim$6″ in the three short-wavelength bands and 12″ in the 22 $\mu$m band, is relatively poor compared to ground-based and space-based infrared observations; e.g., it is 3× larger than that of *Spitzer*-IRAC imaging. For nearby galaxies, the internal structures are smeared and strongly blended from the nucleus to the disk boundary; consequently, it is a challenge to decompose the internal anatomy or to make a detailed comparison with ground-based imaging (e.g., H$\alpha$ line maps) and S4G IRAC imaging. Except for the few largest galaxies, only the global properties are easily obtained from nominal *WISE* imaging. We can, however, recover information that is lost within the *WISE* primary beam using deconvolution methods. These take full advantage of the relatively stable and well-characterized PSF of *WISE*. The first method is the widely used Variable-Pixel Linear Reconstruction, or "drizzle" technique of co-addition, where we employ a modest top-hat kernel (drizzle factor of unity) to reconstruct the mosaics. The second is a true deconvolution technique, detailed below.

The WSDC has developed a generic co-addition and resolution enhancement (HiRes) tool specifically designed to operate on *WISE* single-exposure image frames. This tool produces science-quality image products with statistically validated uncertainty estimates on fluxes. The HiRes algorithm is based on the MCM of Masci & Fowler (2009) and is an extension of the classic Richardson–Lucy deconvolution algorithm, originally implemented to boost the scientific return from *IRAS* approximately 20 years ago (Aumann et al. 1990; Fowler & Aumann 1994; Cao et al. 1997), and is still provided as an online service to users.[16]

The scientific purpose of MCM-HiRes is to significantly enhance the spatial resolution of images while also conserving the integrated flux and maintaining photometric integrity with the extended, low surface brightness emission. Figure 1

qualitatively demonstrates both requirements; after resolution enhancement the *WISE* imaging of the galaxy NGC 1566 is greatly improved (panel 1 versus 2) and resembles the *Spitzer* IRAC+MIPS-24 composite of the galaxy (panel 3). The spiral arms, filaments, and lower surface brightness features in the *WISE* HiRes image are also seen in the *Spitzer* composite; there are no obvious artifacts or isolated features that are unique to the HiRes image relative to *Spitzer*. The images are shown with four colors, where each color is assigned to a *WISE* band: blue $\leftrightarrow$ W1 (3.4 $\mu$m), cyan $\leftrightarrow$ W2 (4.6 $\mu$m), orange $\leftrightarrow$ W3 (12 $\mu$m), and red $\leftrightarrow$ W4 (22 $\mu$m). Stellar light from the old, evolved population will appear blue/green and tends to concentrate in the nucleus and bulge regions. The interstellar medium, warmed and excited by star formation, will appear yellow/orange, delineating H II and photodissociation regions (PDRs) as well as warm dust emission (red) from the disk. Later (Section 5), we conduct a quantitative comparison between *WISE*, *Spitzer*, and *GALEX*.

The overall goal of MCM is to yield a "model" of the sky that is consistent with the observations to within measurement error; see Figure 2. The baseline algorithm assumes no prior information or regularizing constraints like in previous approaches, although use of prior (e.g., cross-wavelength) information is optional. MCM allows for non-isoplanatic (spatially varying) PSFs, noise-variance weighting, a posteriori uncertainty estimation, ringing suppression,[17] statistically motivated convergence criteria and metrics to assess the quality of HiRes solutions, and use of redundant overlapping exposures to optimize the signal-to-noise ratio (S/N). The tool also includes preparatory steps such as background-level and photometric-throughput matching, and outlier/bad-pixel detection and masking. To follow, we validate its performance with simulations and then with real imaging from *WISE* that is compared with *Spitzer*, *GALEX*, and ground-based imaging.

#### 4.1. Simulations

We have explored the impact of the MCM process on photometric flux and noise measurements extracted from resolution-enhanced images using simulations. A simulation here is useful

---

[16] http://irsa.ipac.caltech.edu/IRASdocs/hires_over.html

[17] Like most deconvolution methods, MCM can lead to ringing artifacts in the reconstructed image. This limits super-resolution, i.e., when attempting to go well beyond the diffraction limit of an imaging system.
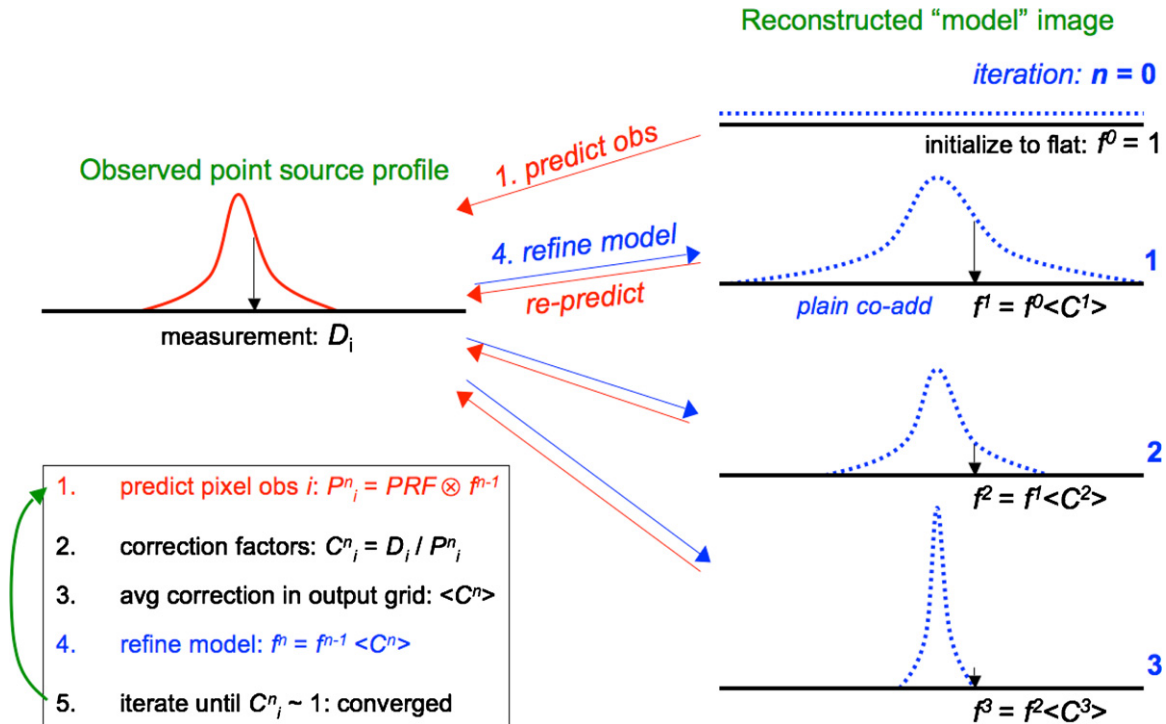
**Figure 2.** Illustrating the iterative deconvolution process of the maximum correlation method, an extension of the classic Richardson–Lucy iterative algorithm. At each iteration, the model is refined and improved using spatially dependent correction factors $C$ such that the "convolved model" reproduces the measurements within the noise, equivalent to $C$ converging to unity.

(A color version of this figure is available in the online journal.)

for two reasons: First, it enables us to validate the accuracy of outputs given knowledge of the truth, and second, it provides us with a method for unambiguously computing the output noise (in response to the input) by simulating repeated noise realizations sampled from a known input noise-distribution model. The simulation uses a single input image with input/output pixel sizes similar to that used in the processing of the *WISE* images in this work and Paper II. We assumed a spatially flat background of 30 DN and added a point source of total flux 3000 DN at the center of the image, convolved with the W1 native PSF. We could have used another *WISE* band, but any one band suffices to illustrate the HiRes performance in general. We then added Poisson noise to this image with variance $\sigma^2 = DN/g$, where we assumed an electronic gain factor of $g = 1$ for simplicity. Different input noise models and/or distributions do not change our general conclusions. 500 independent noise realizations (or trials) were simulated for the input image, and each trial was processed through the MCM-HiRes algorithm to seven different iterations: 1, 2, 4, 8, 16, 24, and 32. Output HiRes images at these iterations for a *single* simulation trial are shown in Figure 3. At the top-left of this figure is the input raw simulated image for this trial. We used the same MCM processing parameters as used for the *WISE* image reconstructions in this work and Paper II.

One can see in Figure 3 that at low iterations, the noise becomes spatially correlated, then with increasing iteration, the positive noise spikes and the point source at the center gradually "decorrelate" and sharpen. Here, the point-source FWHM went from $\simeq 5\farcs8$ (raw input simulated image) to $\simeq 1\farcs75$ (iteration 32), equivalent to an increase of $11\times$ in the flux per solid angle at the point-source position.

Figure 4 (left) shows the dependence of the measured point-source flux (using standard aperture photometry) on the number of MCM iterations from the single simulation-trial images and the average over all 500 independent trials at each iteration number. This shows that the measured fluxes are consistent with the true flux (within measurement error) or what one would measure in an "observed" noisy image. This is an important requirement for any deconvolution process. Figure 4 (right) shows the behavior of the photometric S/N and $1\sigma$ uncertainty in the integrated point-source flux (i.e., the single simulation-trial error bars in Figure 4 (left)) as estimated from the standard deviation of measurements over 500 independent trials. In general, the S/N is expected to smoothly decrease monotonically with iteration number. The hump in S/N at iterations 16 and 24 is due to noise in the single-trial flux measurements at these iterations. The decrease in the integrated S/N is a consequence of noise amplification in general with increasing iteration number (red dashed curve in Figure 4 (right)). Noise amplification is most prevalent when the "ringing suppression" option is used in MCM (adopted throughout this work). It leads to an asymmetric noise distribution with positive noise tail that grows progressively with increasing iteration (for details, see Masci & Fowler 2009). However, the observed drop in integrated S/N is relatively small, and is $\approx 6\%$ over 20 MCM iterations—the maximum number of iterations used in this work.

Similarly, Figure 5 illustrates the evolution of the peak-pixel flux of our simulated point source, including its $1\sigma$ uncertainty and S/N as a function of MCM iteration number. All measurements pertain to single simulation trials. It shows the effective rate at which the flux of a point source is forced into its peak with increasing iteration (assuming the *WISE* pixel sampling). The increase in peak-pixel flux is a factor of $\approx 23$ from iterations 1 to 32. Compared to the uncertainties in integrated flux measurements (Figure 4), the relative increase in the peak-flux
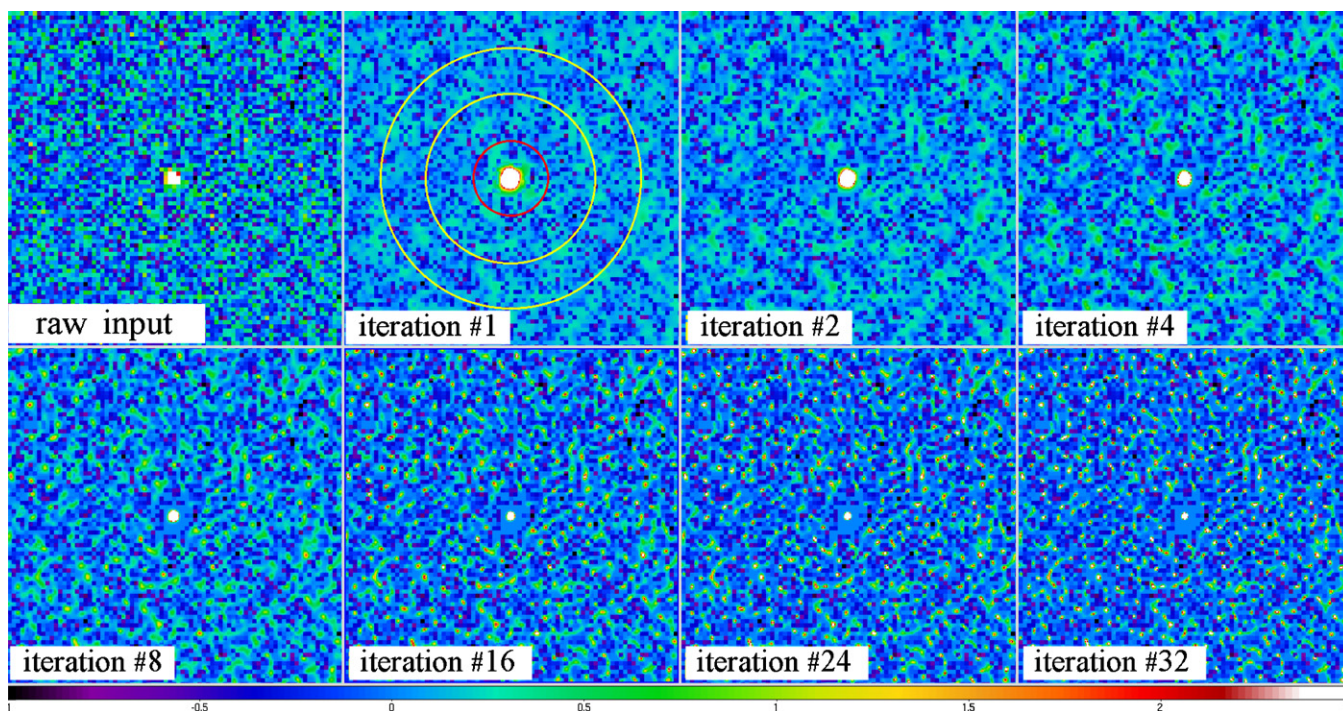
**Figure 3.** Evolution of the pixel noise distribution using the MCM-HiRes technique. A series of intensity images containing simulated Poission noise and a single point source in the middle are shown. The first is the raw input simulated image, followed by the outputs after seven different MCM iterations. These illustrate the evolution of the noise structure. The "iteration 1" output image shows an overlay of the source aperture and background annulus used for the photometric analysis (see Figures 2–5).

(A color version of this figure is available in the online journal.)
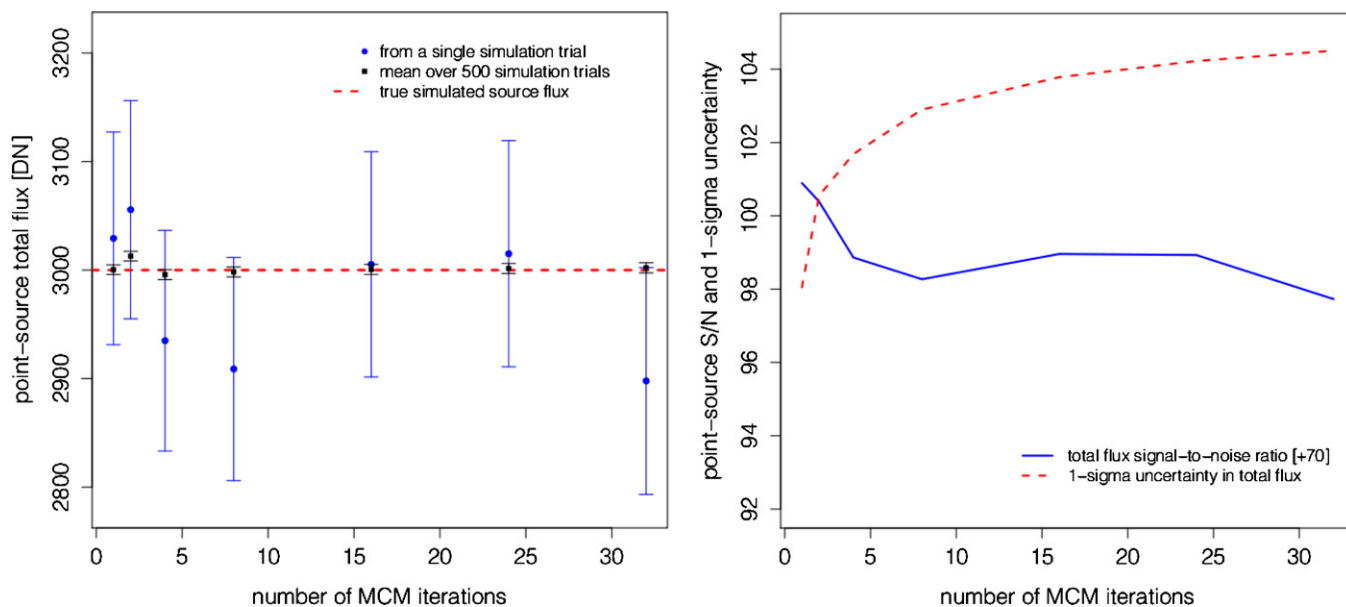


**Figure 4.** Left: total flux of the central point source shown in Figure 3 derived from aperture photometry as a function of iteration number. Measurements were made on image outputs from single simulation trials (blue circles) as well as an averaged stack of 500 trials at each iteration (black squares). The red dashed line shows the true input simulated flux (=3000 DN). These results show that integrated flux measurements made on the HiRes'd images are consistent with the truth (within measurement errors) and hence unbiased. Right: evolution of the signal-to-noise ratio (S/N) with MCM iteration for the single simulation trials (blue curve). An offset of 70 was added for display purposes. Also shown is the $1\sigma$ uncertainty used for the S/N estimates (red dashed curve). This represents the standard deviation in the measured point-source flux (using aperture photometry) over 500 independent simulation trials.

(A color version of this figure is available in the online journal.)

uncertainty with iteration number (Figure 5) is appreciably greater. This implies local (pixel-scale) noise fluctuations are more prone to amplification by the MCM process especially when the ringing suppression option is utilized (see above). Furthermore, we find the amount of amplification depends on

the input noise level. For example, Figure 5 also shows the evolution of the background pixel spatial-rms (dotted curve, ×10 for clarity). The input background (Poisson) noise simulated here is a factor of 8× (in $\sigma$) below that at the point-source peak position, and the background rms varies by only a factor of
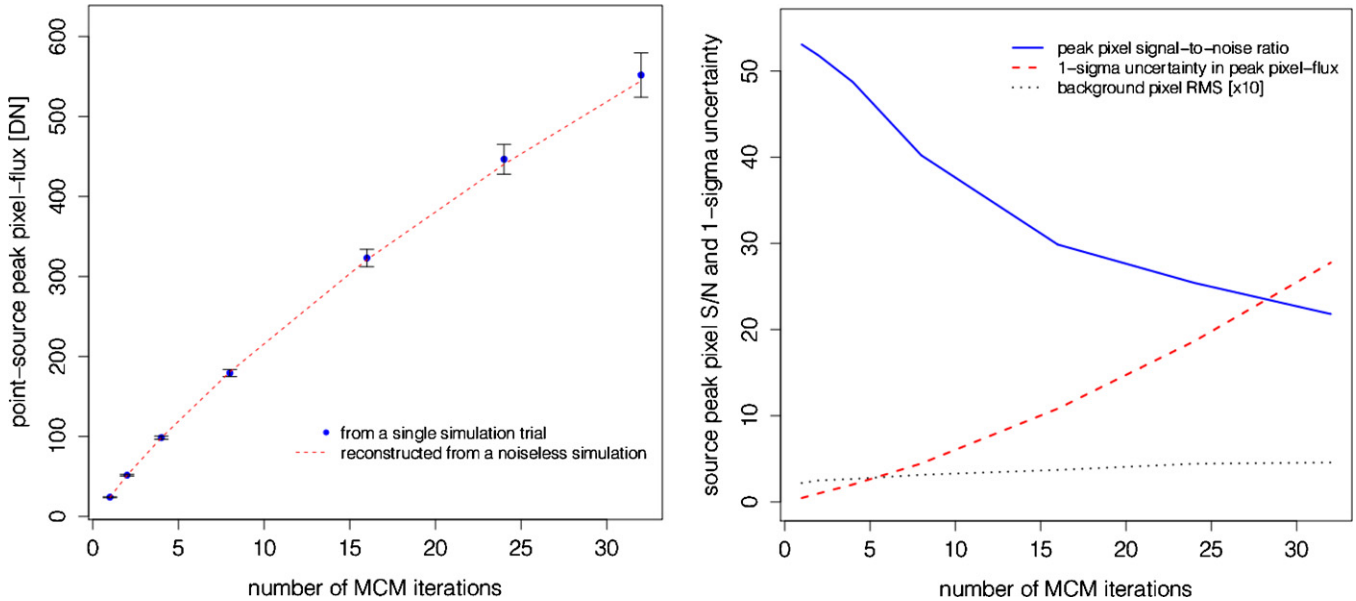
**Figure 5.** Left: flux value in the peak pixel of the point source shown in Figure 3 as a function of iteration number. Measurements were made on image outputs from single simulation trials (blue circles). The red dashed line shows the true reconstructed peak-pixel flux one would obtain if noise were absent. In general, this plot shows the rate at which flux from the wings of a point source is forced into its peak with increasing MCM iteration number. Right: evolution of the peak-pixel S/N ratio with MCM iteration number for the single simulation-trial measurements. The 1σ uncertainty used for these S/N estimates is shown by the red dashed curve. This represents the standard deviation in the measured *peak-pixel* source flux over 500 independent simulation trials. Also shown is the rms in background noise fluctuations (per pixel) vs. iteration number (black dotted curve). The latter were multiplied by 10 for clarity.

(A color version of this figure is available in the online journal.)

≈2 from iterations 1 to 32. Meanwhile, the peak-pixel 1σ flux uncertainty varies by a factor of ≃60 over the same iteration interval. This shows that MCM is inherently a nonlinear process in the reconstruction of signals in the presence of noise.

To summarize, MCM-HiRes is capable of generating science-quality image products with uncertainty estimates on fluxes. Testing on *Spitzer* and *WISE* imaging has shown that it can achieve a factor of ∼3 increase in resolution per axis (using 10–20 iterations), corresponding to at least an order of magnitude increase in flux per unit solid angle (Figure 1; see also Paper II). The gain in resolution improves with increasing survey depth-of-coverage since multiple frame overlaps will provide better sampling of the PSF. Nonetheless, the PSF at all *WISE* bands is sampled at slightly better than the Nyquist rate so that optimal enhancement will be possible at even the lowest depths-of-coverage. Next, we look in more detail at the HiRes performance for NGC 1566.

### 5. HiRes PERFORMANCE: CASE STUDY OF NGC 1566

The nearby spiral galaxy NGC 1566 ($D = 9.5$ Mpc) is used to demonstrate the resolution gain using the MCM-HiRes deconvolution technique (Section 4). We have constructed HiRes mosaics limiting the total number of iterations to 20 for W1, W2, and W3, and 10 iterations for W4 (due to lower quality sampling and S/N for this channel). For the galaxy sample presented in this work and Paper II, we find that between 10 and 20 reconstruction iterations provide the necessary balance between CPU demands, resolution enhancement, and artifact mitigation (artifact-ringing associated with bright sources). Using a smaller iteration truncation (e.g., 5) still results in significant improvement to the overall beam sharpness and represents a more cautious alternative deconvolution of *WISE* imaging. In comparison to *Spitzer* imaging, the *WISE* HiRes reconstructed images are, in a qualitative sense, remarkably

similar, as shown in Figure 1. Note that NGC 1566 was well covered by *WISE*, due to its location at high ecliptic latitude, and thus we expect even better performance with this galaxy; the performance gain from a more diverse set of galaxies is presented in Paper II. Here we consider narrower point-source profiles in the field of the NGC 1566 galaxy, the improved spatial resolution of the galaxy in comparison to the Atlas and "drizzle" co-addition images of *WISE*, and the performance with extended emission and lower surface brightness features.

The improvement in the spatial resolution, as traced by the radial profiles of foreground stars located near NGC 1566, is shown in Figure 6. The *WISE* "drizzled" image results are shown with the dashed gray line, and the solid black line shows the MCM-HiRes results for a point source. Table 1 summarizes the widths of point sources. The Atlas imaging (dotted gray line), optimized for point-source detection, has relatively poor angular resolution as gauged by the mean FWHM: 8″.4, 9″.2, 11″.4, and 18″.6 for W1, W2, W3, and W4, respectively. Significant improvement is gained through simple top-hat drizzle imaging; widths are found to be 5″.9, 6″.5, 7″.0, and 12″.4 for W1, W2, W3, and W4, respectively. Finally, the greatest improvement is derived from the MCM-Hires deconvolution: 2″.6, 3″.0, 3″.5, and 5″.5, for W1, W2, W3, and W4 widths, respectively. At the distance of 9.5 Mpc, the HiRes is sampling physical scales down to 120 pc. Figure 6 also shows the PSF beams for SINGS-drizzled IRAC and MIPS-24 imaging, and the *GALEX* NUV and *B*-band imaging. In the case of IRAC, the FWHM is 2″.1, 2″.2, and 2″.3 for IRAC-1, IRAC-2, and IRAC4, respectively. The MIPS-24 beam FWHM is 5″.2. The *GALEX* NUV has an effective beam FWHM of 4″.8, while the optical *B*-band image has relatively good seeing, FWHM = 1″.3. It is clear that improvement in spatial resolution is significant for the *WISE* imaging, achieving scales that are similar to those of *Spitzer* imaging, and at the shorter wavelengths better than those of *GALEX*. Next, we inspect the performance on the galaxy itself.
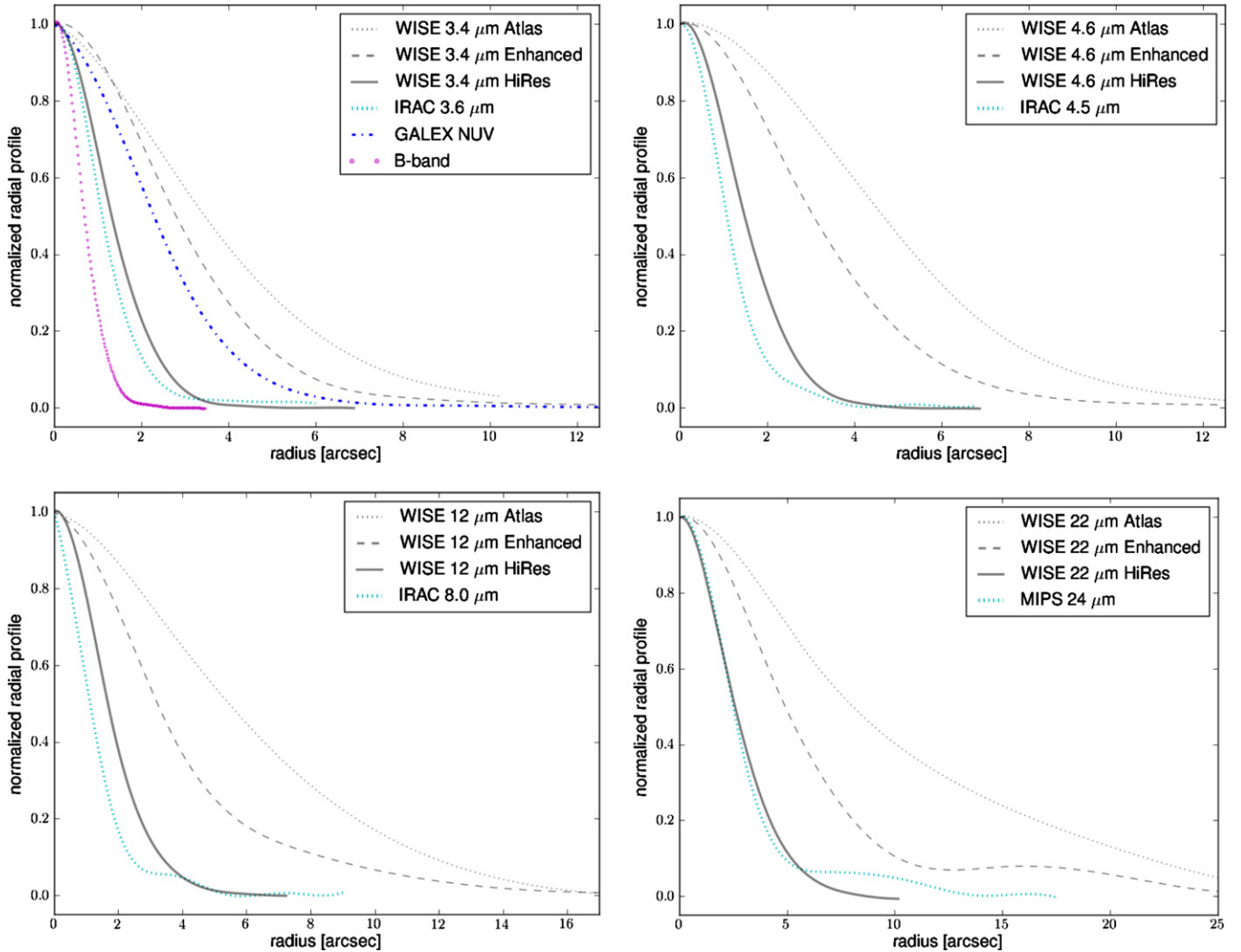
**Figure 6.** Azimuthally averaged radial point-source profiles, comparing *WISE* (Atlas, drizzle-enhanced, and HiRes) with IRAC, *GALEX*, and optical ground-based imaging. The panels are separated by the *WISE* bands: 3.4, 4.6, 12, and 22 $\mu$m. The dotted gray line represents the Atlas profile, the dashed gray line represents the enhanced-drizzle profile, and the solid black line represents the MCM-HiRes profile.

(A color version of this figure is available in the online journal.)

Figure 1 shows a color composite of all *WISE* bands simultaneously, comparing the nominal Atlas to HiRes performance. Decomposing into the individual components (Figure 7) the HiRes improvement (lower panels) is clearly evident across all bands: the spiral arms, disk star formation aggregates, and circumnuclear regions are revealed. The improvement in angular resolution is approximately a factor of 3–4, with the resulting FWHM $\sim 3''$ for W1, W2, and W3, and $\sim 6''$ for W4.

Another way to view the relative improvement in performance at large scales is through one-dimensional slices, cutting across the nucleus and spiral arms north and south of the center (see Figure 8). To gauge the resolution fidelity of the *WISE* HiRes, also shown are the corresponding slices through IRAC and MIPS-24. Roughly five different spiral arms are crossed by the horizontal cuts. Discrete structures are more sharply delineated with HiRes and IRAC, while the overall mean surface brightness is conserved (see also Figure 9 below, showing the radial, azimuthal average).

In particular, W3 is notably improved; the strong neutral polycyclic aromatic hydrocarbon (PAH) emission arising within the spiral arms and tracing star formation regions creates the sawtooth pattern in the slices and nucleus, and inter-arm and spiral-arm features in the azimuthal average. All of these features are seen in the IRAC profiles, validating the reconstruction. W4 shows an unavoidable consequence of the MCM-HiRes method: the formation of dark (lower intensity) troughs around regions with bright, rapidly varying emission on compact spatial scales. Much lower amplitude troughs appear in the MIP-24 image, verifying that the W4 HiRes does have this artifact feature. For example, note the cut through the bright nucleus (W4 panel of Figure 8), likewise seen in the azimuthal average of the radial surface brightness, where the W4 panel of Figure 9 shows the circular "ring" trough at a radius $\sim 15''$. At small scales, the flux is conserved within a circular area that encompasses the source and "ring." Although this "ringing" phenomenon is minimized in the current HiRes method, it is strongest in the W4 reconstructions due to the relatively earlier onset of saturation that can modify source profiles compared to the native PSF. The higher background in general also has an impact on the ringing that is introduced into the reconstruction. Caution is required when interpreting the W4 light distribution in proximity to bright sources (stars, nuclei, etc.); nevertheless, as we show in Section 4.1, the overall W4 integrated flux is conserved and the reconstructions maintain science-level quality.
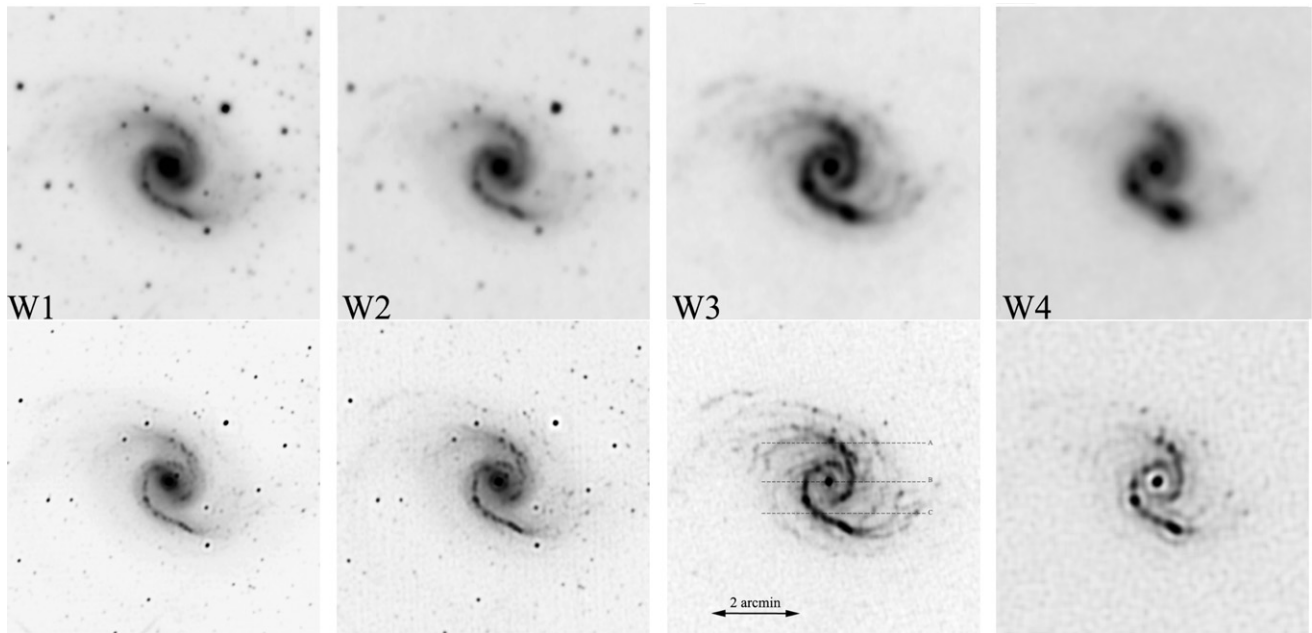
**Figure 7.** *WISE* view of NGC 1566. The top panels show the 3.4 μm, 4.6 μm, 12.0 μm, and 22 μm channels with nominal (Atlas) *WISE* mosaic construction. The bottom panels show the same mosaics after MCM spatial resolution enhancement. The dashed lines (A, B, and C) shown in the W3 panel denote the location of the line profile comparisons between nominal and high resolution presented in Figure 8.
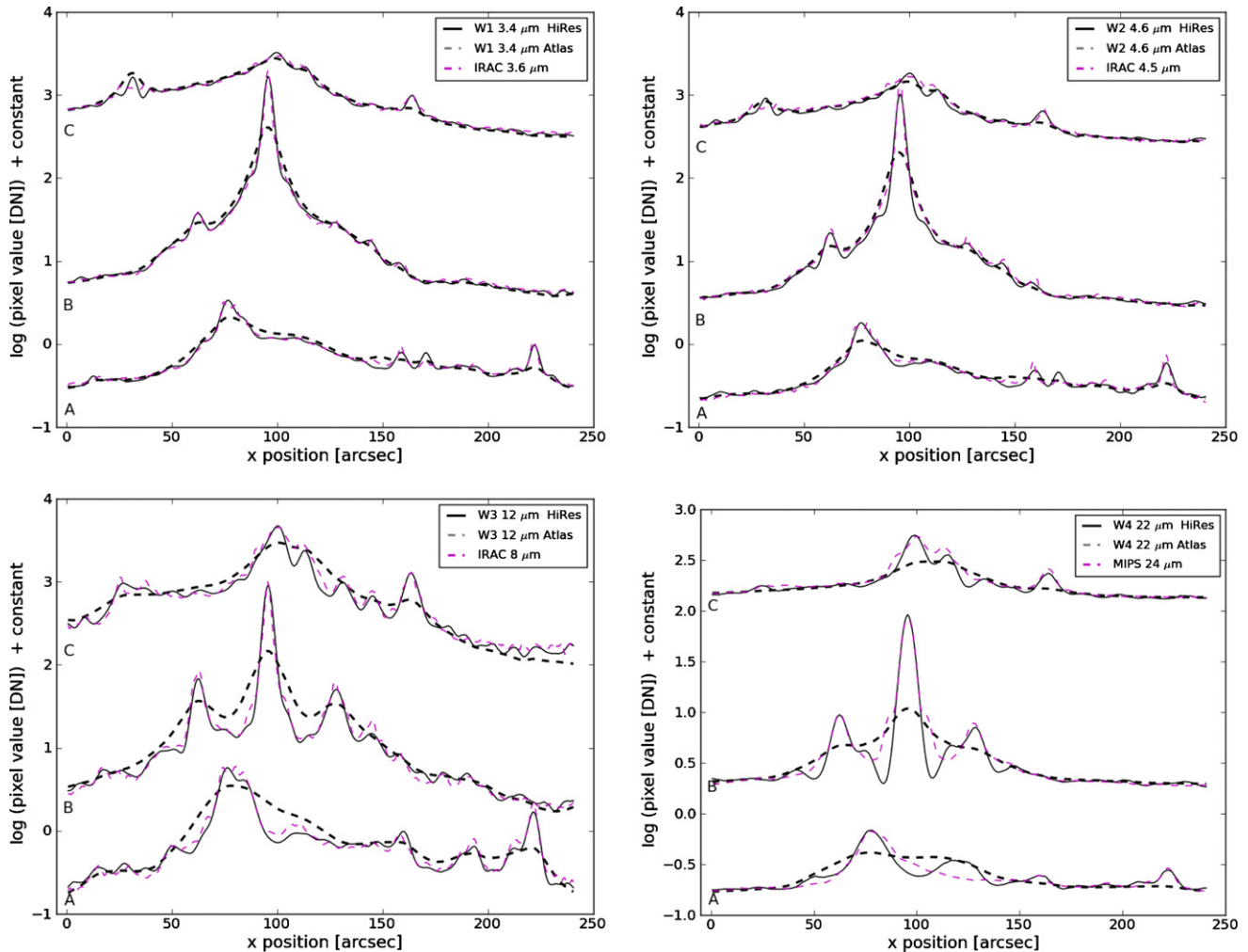


**Figure 8.** One-dimensional line profile comparison between the Atlas/nominal (dashed line), high-resolution (solid line), and *Spitzer* IRAC or MIPS-24 (magenta dashed) imaging of NGC 1566. Three profiles or line-cuts are shown, labeled A, B, C; Figure 7 specifies the regions, with the center profile (B) slicing across the nucleus and spiral arms.

(A color version of this figure is available in the online journal.)
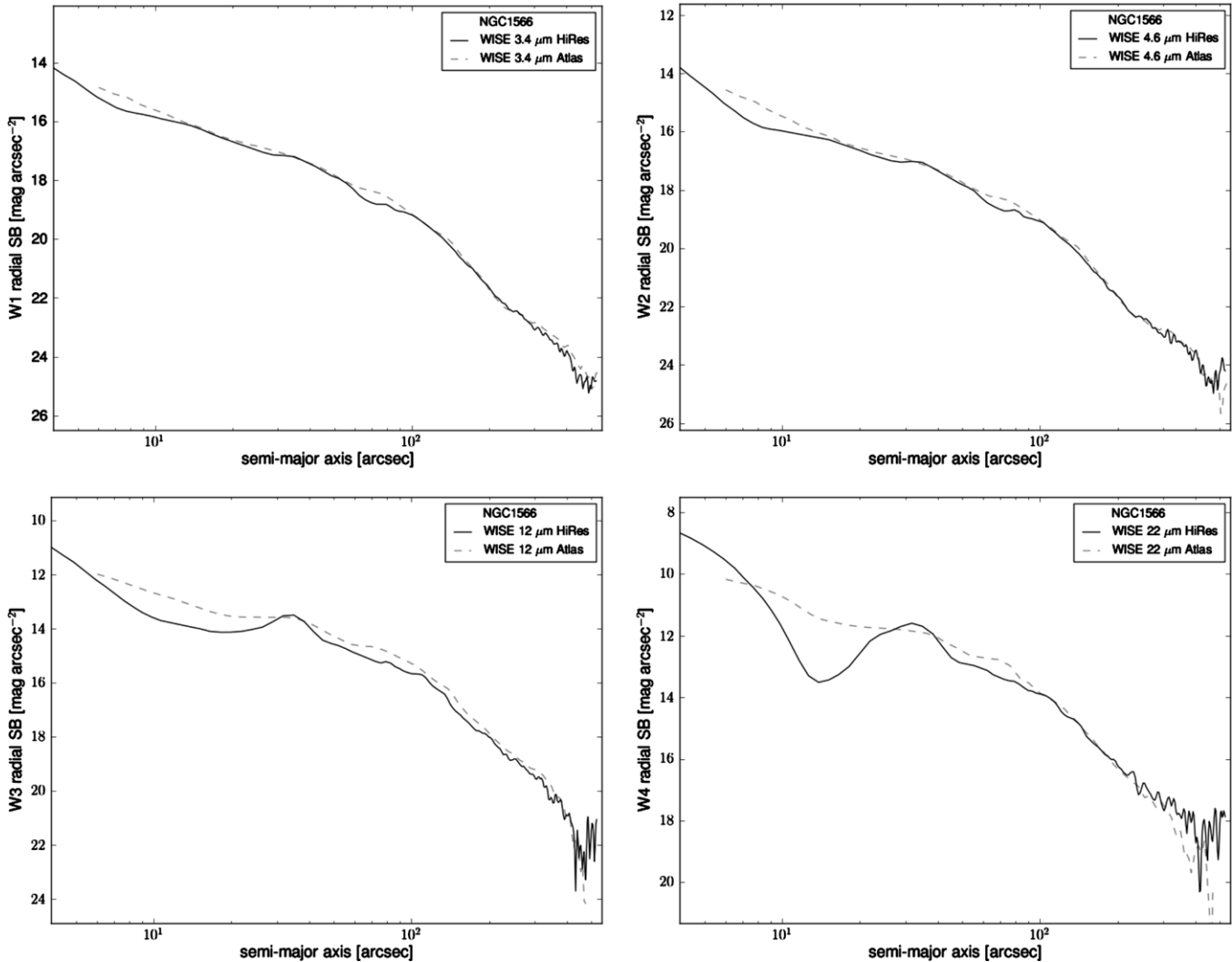
**Figure 9.** *WISE* azimuthally averaged elliptical–radial profile of NGC 1566. For comparison, the nominal (Atlas) resolution and the high (HiRes) resolution are shown for each band.

At yet larger scales, we investigate the relative performance by azimuthally averaging the surface brightness, comparing the resultant radial profiles. The local background was derived using an annulus with an inner radius of $6'.7$ and a width of $0'.3$ (data reduction is discussed in detail in Paper II). Figure 9 shows the radial profiles extending down to the local background level, roughly 24.9, 24.5, 22.1, and 18.3 mag arcsec$^{-2}$ for W1, W2, W3, and W4, respectively. The only significant difference between the Atlas and HiRes radial profiles are the better resolved spiral arms and nuclear regions, notably for the star formation sensitive W3 and W4 bands. At low surface brightnesses, the HiRes is clearly conserving flux relative to the Atlas images.

We now compare the *WISE* Atlas and HiRes radial surface brightness profiles to those measured using *Spitzer* and *GALEX* imaging. Figure 10 presents the surface brightness for *WISE* (W1 and W2) and *Spitzer* (IRAC-1 and IRAC-2), and the addition of *GALEX* (NUV) to the W3+IRAC-4 profiles and *GALEX* (FUV) to the W4+MIPS-24 profiles. The *WISE* and *Spitzer* magnitudes are in standard Vega units, and the *GALEX* magnitudes are in AB units plus an offset of −7 mag to fit within the plot limits.

The first panel shows that W1 3.4 $\mu$m and IRAC-1 3.6 $\mu$m have very similar profiles, both easily reaching depths of ~24 mag arcsec$^{-2}$ (corresponding to 26.7 mag arcsec$^{-2}$ in AB).

The profiles are smooth, tracing the old stellar populations that form the spheroid spatial distribution. The second panel shows the W2 4.6 $\mu$m and IRAC-2 4.5 $\mu$m profiles, which are also nicely co-aligned. The W2 and IRAC-2 depth reaches a similar limit of ~24 mag arcsec$^{-2}$ (corresponding to 27.3 mag arcsec$^{-2}$ in AB). Both of these short-wavelength sets, W1/IRAC-1 and W2/IRAC-2, have bandpasses that are similar enough that less than 5%–10% deviations are expected due to spectral differences (detailed band-to-band analysis is presented in Paper II). The third panel shows the W3 12 $\mu$m, IRAC-4 8 $\mu$m, and *GALEX* NUV + FUV. Both W3 and IRAC-4 have the same shape (radius < 150″), but are offset slightly due to band-to-band differences between *WISE* and *Spitzer*: We would expect a flux ratio of 1.1 for late-type galaxies (see Paper II). Also, the IRAC-4 8 $\mu$m surface brightness is falling rapidly beyond a radius of 200″, likely due increased noise and an asymmetric background gradient that is created by scattered light and detector muxbleed from a nearby bright star (see Figure 1; also see Figure 11 below). The W3 depth reaches a limit of 22 mag arcsec$^{-2}$ (corresponding to 27.2 mag arcsec$^{-2}$ in AB). In the UV window, the profiles have considerably different shapes; notably, the absence of UV emission in the central core (note the shallow profiles out to a radius of 20″ radius) and the spiral arms shifted outward by 15″–20″ (~0.9 kpc), exhibiting
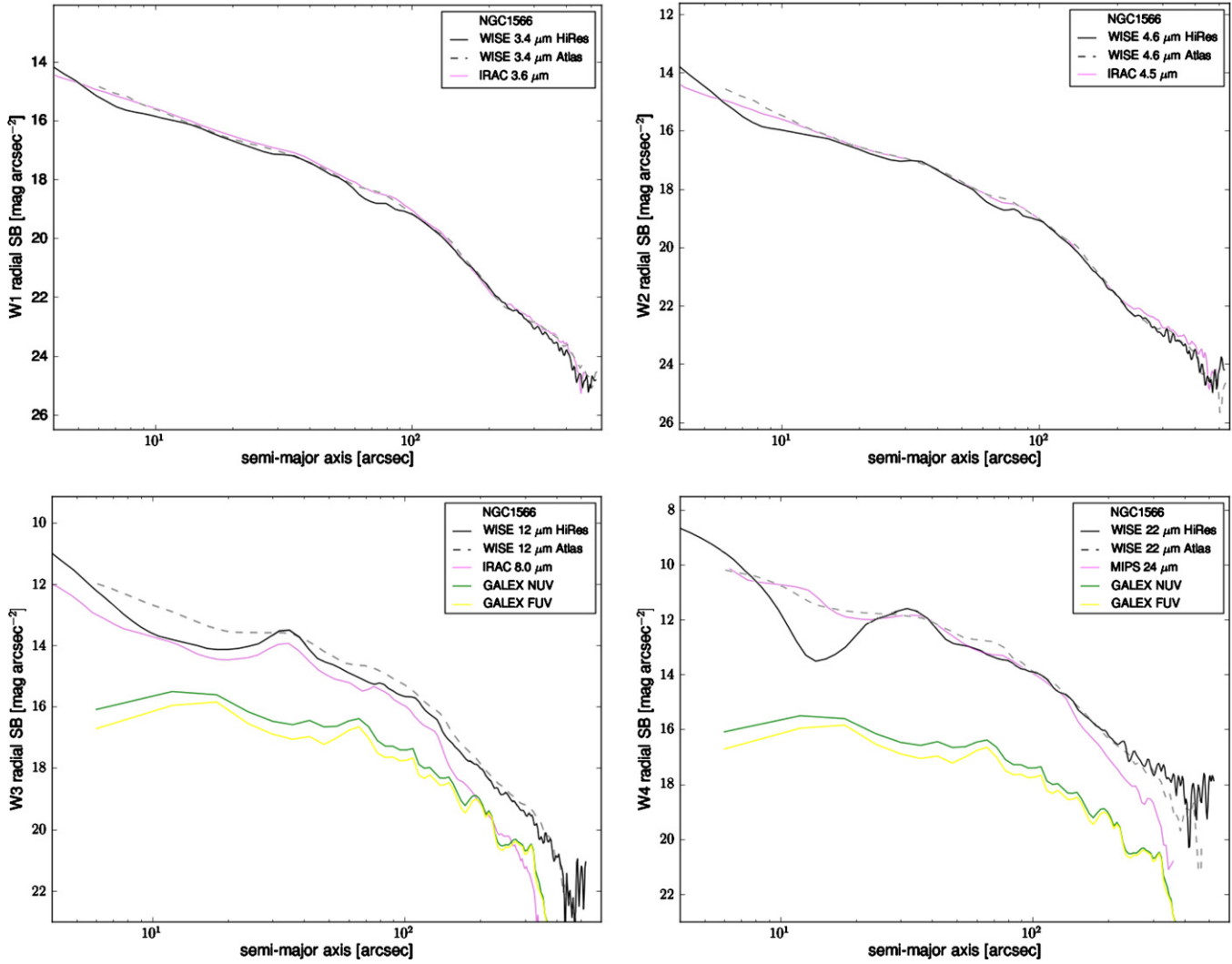
**Figure 10.** NGC 1566 radial profile comparison between *WISE* HiRes, *WISE* Atlas, *Spitzer*, and *GALEX*. The units are Vega mag arcsec$^{-2}$. For the W3 and W4 panels, the *GALEX* AB magnitudes have been offset by $\sim$7 mag to fit within the *Y*-axis dynamic range.

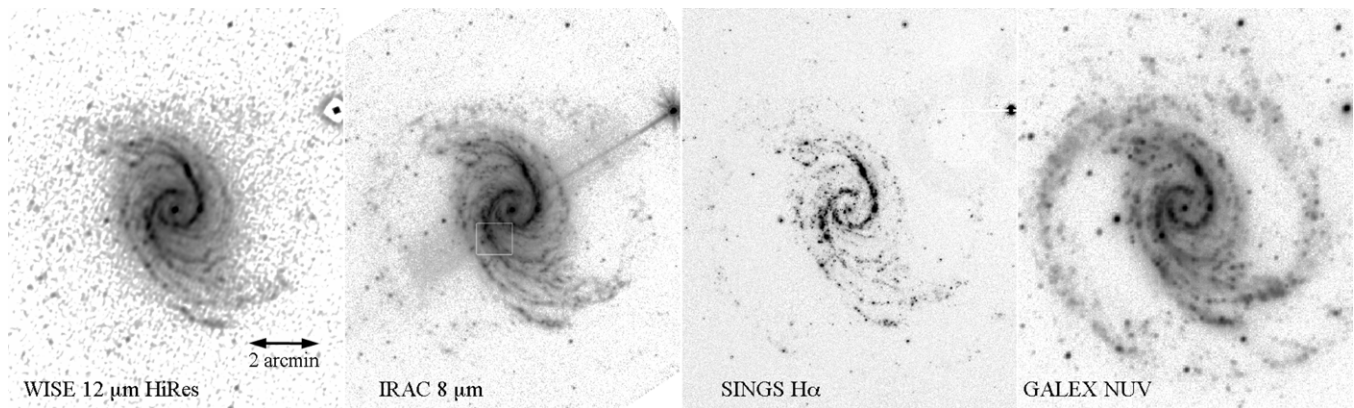(A color version of this figure is available in the online journal.)



**Figure 11.** Mapping the star formation in NGC 1566 using infrared, ultraviolet, and H$\alpha$ tracers. From left to right: *WISE* 12 $\mu$m HiRes, *Spitzer*-IRAC 8 $\mu$m, optical H$\alpha$ (0.656 $\mu$m), and *GALEX* NUV (0.227 $\mu$m) imaging. The small white box in the second panel denotes the region that is highlighted in Figure 12.

a more pronounced, localized or compact, signal relative to the infrared. The UV light then falls off steeper than the infrared light between 300″ and 400″, but then dramatically extends well beyond (>500″) the infrared signal, forming an additional set of arms that are invisible to *WISE* and barely seen in IRAC-4

(see below, Figure 11). The last panel shows the W4 22 $\mu$m, MIPS 24 $\mu$m, and *GALEX* NUV + FUV. W4 HiRes exhibits sharper profiles than MIPS-24 (note the dip at 156″) and exhibits higher surface brightness at larger radii (>200″). The W4 Atlas profile appears to better track the MIPS-24 profile. Note that
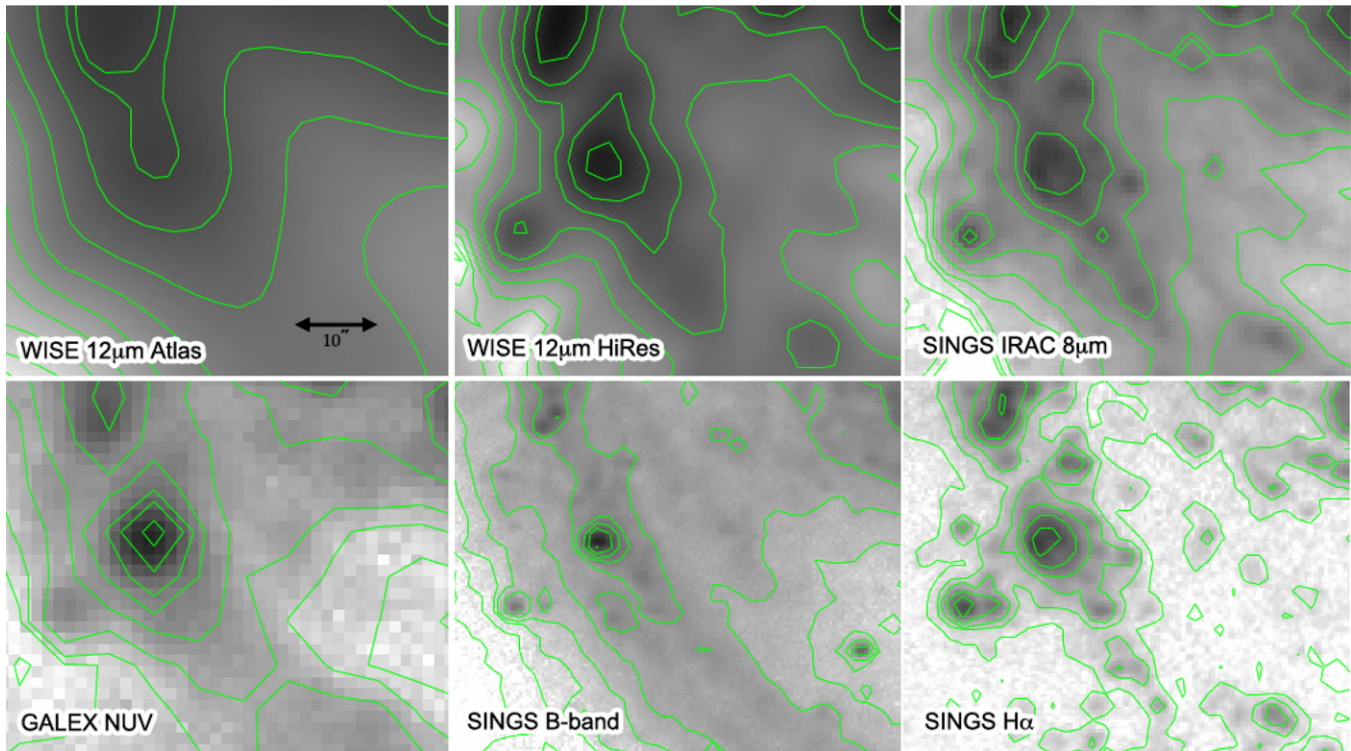
**Figure 12.** Southeastern spiral arm of NGC 1566, centered on R.A. = 04:20:04, decl. = −54:57:03 (see Figure 11). The gray-scale images show the star formation sensitive bands of *WISE* 12 $\mu$m, *Spitzer*-IRAC 8 $\mu$m, *GALEX* NUV (0.227 $\mu$m), optical *B* band (0.44 $\mu$m), and optical H$\alpha$ (0.656 $\mu$m). The green contours are used to enhance the star formation structures captured in the imaging. The 10″ angular scale corresponds to a physical scale of 460 pc.

(A color version of this figure is available in the online journal.)

MIPS-24 is also subject to a background gradient that is limiting the extraction at faint depths. The W4 depth easily reaches a limit of 18.5 mag arcsec$^{-2}$ (corresponding to 25.1 mag arcsec$^{-2}$ in AB). Likewise with the W3 comparison to the UV, the W4 band appears shifted relative to the *GALEX* bands, although it is not as distinct as 12 $\mu$m comparison.

The final set of comparisons to be made in this NGC 1566 analysis is concerned with the smallest scales. To demonstrate the power of HiRes and its ability to tease out structure at small scales, we zoom into the southeastern inner spiral arm. Figure 11 shows the star formation sensitive imaging of NGC 1566: *WISE* 12 $\mu$m HiRes which is tracing the 11.3 $\mu$m PAH emission (predominantly arising from PDRs), *Spitzer*-IRAC 8 $\mu$m, which is tracing the 6.2 and 7.7 PAHs, optical H$\alpha$, which traces recombination in H II regions, and *GALEX* NUV (0.227 $\mu$m), which traces the high-energy stellar emission. Both the H$\alpha$ and the NUV are tracing the youngest, most massive populations, while the infrared arises from obscured star formation from both massive and intermediate-mass stars.

The spiral arms and high surface brightness knots/filaments, where the newly forming stars are primarily concentrated, are clearly delineated for all four tracers. Note the sensitivity of the *GALEX* image, easily detecting the outer spiral arm of this galaxy (yet invisible to *WISE* and nearly so to IRAC). Zooming into the southeastern arm (as denoted in the 2nd panel), the smallest scales that the imaging provides are shown in Figure 12.

Six panels are shown in Figure 12: The upper panels represent the obscured star formation, and the lower panels the unobscured star formation. The *WISE* Atlas image is smooth and mostly featureless due to its poor angular resolution, washing out the spiral arm and dense star formation complexes. The situation is

greatly improved after MCM super-resolution treatment; the *WISE* image is now delineating the spiral arm into several components. The overall and detailed morphology that the *WISE* HiRes image is revealing is validated and confirmed with the *Spitzer*-IRAC 8 $\mu$m image. The knots, gradients, and shape of the region that are revealed in *WISE* are easily seen in *Spitzer*: This confirms that the MCM process is stable and reliable, recovering spatial information that is astrophysical and real. Comparing to the unobscured, massive star formation tracers (lower panels), the primary site of star formation (high surface brightness features) is cospatial. The H$\alpha$ image, with its superior angular resolution, resolves many of these bright knots into smaller components (on physical scales the size of giant molecular clouds), but is only sensitive to the high surface brightness population (H II regions). Both the infrared and NUV trace more diffuse emission that is associated with star formation from less massive (yet far more numerous) stars.

The nominal *WISE* Atlas images are fully adequate to study the global characteristics of galaxies (see, e.g., Figure 9), but as Figure 12 clearly demonstrates, the HiRes technique is crucial if *WISE* is to be used to study the detailed anatomy of galaxies. As a final demonstration, we now combine the power of the *WISE* bands to understand galaxy evolution. The W1 (and W2) band is sensitive to the dominant mass component of (most) galaxies, namely, the evolved stellar population. In contrast, the W3 (and W4) is sensitive to the present-day star formation activity. Combining the two creates a metric that is used to assess the present to past star formation history. This metric is also known as the specific star formation rate (sSFR), generally stated as the ratio of the SFR to the stellar mass ($M_*$). For this demonstration, we simply ratio the W3 image (which is proportional to the SFR,
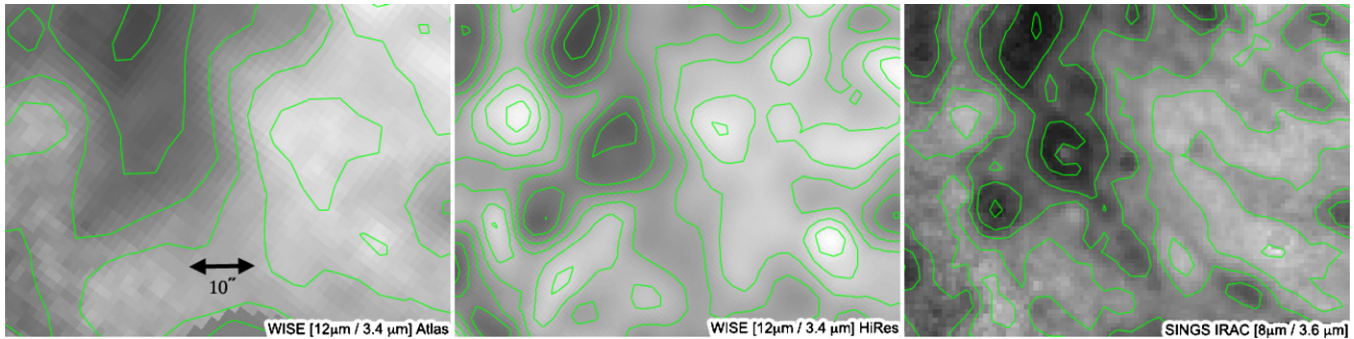
**Figure 13.** Tracing the specific star formation rate (sSFR) in the southeastern spiral arm of NGC 1566. The proxy for the star formation rate is the mid-infrared (PAH) emission, while the stellar mass is traced by the near-infrared emission. Accordingly, we construct a (proportional) sSFR using the ratio of the *WISE* 12–3.4 $\mu$m imaging, and the IRAC 8–3.6 $\mu$m imaging. See Figure 12 for coordinate and scale information.

(A color version of this figure is available in the online journal.)

as detailed in Paper II) to the W1 image (which is proportional to $M_*$ plus a color term, detailed in Paper II). The result is shown in Figure 13, where we are comparing the *WISE* sSFR with the equivalent *Spitzer* sSFR (IRAC 8 to 3.6 $\mu$m ratio). It is no surprise that the *WISE* Atlas result is mostly washed out, only painting a gentle gradient across the field (i.e., the spiral arm itself). The HiRes result, however, reveals several concentrations of high sSFR (as confirmed by the *Spitzer* result). These regions of enhanced sSFR are precisely where the galaxy is creating new building blocks, where it is actively building its disk. In contrast, the low sSFR regions, dominated by the inner-arm regions, are currently quiescent and filled with older, evolved stars. A metric such as the sSFR demands the highest resolution possible since it is a ratio of two separate images, and only *WISE* HiRes provides enough information to study the details star formation evolution in galaxies.

As a final note to the analysis presented in this work, NGC 1566 is not an exception, and the spatial resolution improvement from MCM-HiRes is realized for all of the galaxies in the sample presented in Paper II, which assesses the photometric performance of the reconstructed images in comparison to *Spitzer* photometry.

## 6. SUMMARY

In this paper we have presented a method by which to recover spatial information and significantly improve the angular resolution of *WISE* mid-infrared imaging, enabling detailed study of the internal anatomy of galaxies. Developed by the WSDC, the MCM yields improvements that are 3–4 times better than the nominal *WISE* Atlas imaging resolution, and factors of 2–3 times improvement from standard "drizzle" co-addition. Using the nearby galaxy NGC 1566 as a case study, we demonstrate how the angular resolution of *WISE* may be robustly enhanced to achieve information on physical scales comparable to those of *Spitzer* imaging. This method will be used to construct the WHRGA, consisting of several thousand nearby galaxies. A pilot study is now underway; the initial results derived from a sample of 17 large, nearby galaxies are presented in a companion paper.

## REFERENCES

Aumann, H. H., Fowler, J. W., & Melnyk, M. 1990, AJ, 99, 1674
Cao, Y., Tereby, S., Prince, T. A., & Beichman, C. A. 1997, ApJS, 111, 387
Cutri, R., et al. 2012, Explanatory Supplement to the *WISE* All-sky Data Release Products, http://wise2.ipac.caltech.edu/docs/release/allsky/expsup/
Fowler, J. W., & Aumann, H. H. 1994, in Science with High-Resolution Far-Infrared Data, ed. S. Terebey & J. Mazzarella (JPL Publication 94-5), 1
Jarrett, T. J., Cohen, M., Masci, F., et al. 2011, ApJ, 735, 112
Jarrett, T. J., et al. 2012, AJ, submitted (Paper II)
Kennicutt, R., Armus, L., Bendo, G., et al. 2003, PASP, 115, 928
Martin, D. C., Fanson, J., Schiminovich, D., et al. 2005, ApJ, 619, L1
Masci, F. J., & Fowler, J. W. 2009, in ASP Conf. Ser. 411, Proceedings of Astronomical Data Analysis Software and Systems XVIII, Quebec City, ed. D. Bohlender, P. Dowler, & D. Durand (San Francisco, CA: ASP), 67
Morrissey, P., Conrow, T., Barlow, T. A., et al. 2007, ApJS, 173, 682
Morrissey, P., Schiminovich, D., Barlow, T. A., et al. 2005, ApJ, 619, L7
Murakami, H., Baba, H., Barthel, P., et al. 2007, PASJ, 59, S369
Sheth, K., Regan, M., Hinz, J. L., et al. 2010, PASP, 122, 1397
Tully, R. B. 1988, Nearby Galaxy Catalog, VizieR On-line Data Catalog: VII/145 (Cambridge: Cambridge Univ. Press)
Willick, J. A., Courteau, S., Faber, S. M., et al. 1997, ApJS, 109, 333
Wright, E., Eisenhardt, P. R. M., Mainzer, A. K., et al. 2010, AJ, 140, 1868